




The role of critical micellization concentration in efficacy and toxicity of supramolecular polymers

Hao Su^{a,b,1}, Feihu Wang^{a,b,1}, Wei Ran^c, Weijie Zhang^{a,b,d}, Wenbing Dai^{a,b,e}, Han Wang^{a,b}, Caleb F. Anderson^{a,b}, Zongyuan Wang^{a,b,f}, Chao Zheng^c, Pengcheng Zhang^c, Yaping Li^c, and Honggang Cui^{a,b,g,h,i,2} 

^aDepartment of Chemical and Biomolecular Engineering, The Johns Hopkins University, Baltimore, MD 21218; ^bInstitute for NanoBioTechnology, The Johns Hopkins University, Baltimore, MD 21218; ^cState Key Laboratory of Drug Research and Center for Pharmaceutics, Shanghai Institute of Materia Medica, Chinese Academy of Sciences, Shanghai 201203, China; ^dDepartment of Oncology, The First Affiliated Hospital of Zhengzhou University, Zhengzhou 450052, Henan, China; ^eBeijing Key Laboratory of Molecular Pharmaceutics and New Drug Delivery Systems, School of Pharmaceutical Sciences, Peking University, Beijing 100191, China; ^fCollaborative Innovation Center of Chemical Science and Engineering, School of Chemical Engineering and Technology, Tianjin University, Tianjin 300072, China; ^gCenter for Nanomedicine, The Wilmer Eye Institute, Johns Hopkins University School of Medicine, Baltimore, MD 21231; ^hDepartment of Oncology, Johns Hopkins University School of Medicine, Baltimore, MD 21205; and ⁱSidney Kimmel Comprehensive Cancer Center, Johns Hopkins University School of Medicine, Baltimore, MD 21205

Edited by Matthew V. Tirrell, The University of Chicago, Chicago, IL, and approved January 21, 2020 (received for review August 7, 2019)

The inception and development of supramolecular chemistry have provided a vast library of supramolecular structures and materials for improved practice of medicine. In the context of therapeutic delivery, while supramolecular nanostructures offer a wide variety of morphologies as drug carriers for optimized targeting and controlled release, concerns are often raised as to how their morphological stability and structural integrity impact their in vivo performance. After intravenous (i.v.) administration, the intrinsic reversible and dynamic feature of supramolecular assemblies may lead them to dissociate upon plasma dilution to a concentration below their critical micellization concentration (CMC). As such, CMC represents an important characteristic for supramolecular biomaterials design, but its pharmaceutical role remains elusive. Here, we report the design of a series of self-assembling prodrugs (SAPDs) that spontaneously associate in aqueous solution into supramolecular polymers (SPs) with varying CMCs. Two hydrophobic camptothecin (CPT) molecules were conjugated onto oligoethylene-glycol (OEG)-decorated segments with various OEG repeat numbers (2, 4, 6, 8). Our studies show that the lower the CMC, the lower the maximum tolerated dose (MTD) in rodents. When administered at the same dosage of 10 mg/kg (CPT equivalent), SAPD 1, the one with the lowest CMC, shows the best efficacy in tumor suppression. These observations can be explained by the circulation and dissociation of SAPD SPs and the difference in molecular and supramolecular distribution between excretion and organ uptake. We believe these findings offer important insight into the role of supramolecular stability in determining their therapeutic index and in vivo efficacy.

critical micellization concentration | molecular assembly | supramolecular polymers | drug delivery | prodrugs

Supramolecular polymers (SPs) formed via noncovalent synthesis can serve as effective carriers for therapeutic or diagnostic agents (1–8). The incorporation of active compounds into supramolecular nanostructures by either physical encapsulation or covalent conjugation preserves the payload's inherent biological characteristics while adding in beneficial traits beyond the individual therapeutic agents (9–15). For example, a poorly water-soluble drug can be encapsulated into the hydrophobic core of SPs that promotes the drug's solubility and improves the performance of the active compound (16, 17). In other examples, pharmaceutically active compounds are conjugated onto an auxiliary segment through biodegradable linkers to create SPs for both systemic and local drug administrations (18–23). This strategy of using drug-bearing amphiphilic molecules to create well-defined SPs in aqueous solutions represents a carrier-free drug delivery approach and also enables precise control over physiochemical properties of SPs from the molecular level (24–33). In these cases, one can tune the release kinetics of payloads by altering the

strength and nature of supramolecular interactions, with additional functionalities readily installed through inclusion of bioactive ligands.

In the design of SPs for all in vivo biomedical applications, critical micellization concentration (CMC) is an important consideration, as it reflects the propensity of the molecular building units to aggregate or dissociate in solution state. In general, self-assembling units start to aggregate above this threshold concentration to form stable, well-defined nanostructures. As a result of the noncovalent nature of interactions that hold the units together, there always exists a dynamic exchange between assemblies and monomers (10, 34). This reversible assembly–disassembly process facilitates the supramolecular formulation of therapeutic agents and also enables their specific responsiveness to biomolecular cues to achieve controlled release at desired sites. However, in cases of therapeutic delivery via intravenous (i.v.) injection where the solution concentration may drop unavoidably upon plasma dilution, concerns rise that these SPs could start to dissociate into monomers and partially lose their well-designed supramolecular characteristics (34, 35). For example, assemblies with too high a CMC value could dissociate quickly in vivo, resulting in a pharmacokinetic profile that has little to nothing to do

Significance

Critical micellization concentration (CMC) is an important design consideration for developing all supramolecular biomaterials, and in particular for drug delivery systems. Once placed in an in vivo setting, supramolecular materials will start to dissociate into monomeric units, providing a means for therapeutic release and an essential pathway for clearance. This beneficial phenomenon could also lead to premature drug release and degradation. Through the design of a series of self-assembling prodrugs (SAPDs) of various CMCs, we developed a fundamental understanding of the role of CMC in therapeutic efficacy of supramolecular polymers. We found that the two important parameters of assessing a drug potential (efficacy and toxicity) can be correlated to the SAPD's supramolecular form and monomeric form, respectively.

Author contributions: H.S. and H.C. designed research; H.S., F.W., W.R., W.Z., W.D., H.W., C.F.A., Z.W., C.Z., and P.Z. performed research; H.S., F.W., P.Z., Y.L., and H.C. analyzed data; and H.S., F.W., and H.C. wrote the paper.

The authors declare no competing interest.

This article is a PNAS Direct Submission.

Published under the PNAS license.

¹H.S. and F.W. contributed equally to this work.

²To whom correspondence may be addressed. Email: hcui6@jhu.edu.

This article contains supporting information online at <https://www.pnas.org/lookup/suppl/doi:10.1073/pnas.1913655117/-DCSupplemental>.

First published February 18, 2020.

with their supramolecular traits. In light of this, there have been some attempts to understand its significance in supramolecular systems (36–39). Tirrell and coworkers (40) reported a self-assembling peptide micelle system containing a cytotoxic T cell epitope with a CMC of 2.2 μM . They found that the micelles incubated with egg phosphatidylcholine liposomes undergo a slow disassociation with a half-life of 38 h, which is much longer than the time (1 to 2 h) for nanoparticle to travel to lymph node. Their results demonstrated the importance of kinetic stability of micellar assemblies to allow sufficient amount of time to exert their biological activities. In another work, the Xu laboratory (41) has shown that the self-assembling ability of small molecules can determine the anticancer activity of enzyme-instructed self-assembly for inhibiting cancer cells. More recently, the Cao group (42) has developed a micellar drug delivery system with ultralow critical micelle concentration of 10^{-6} mM, which shows great efficacy in a mouse melanoma model. These studies revealed the important role of CMC in supramolecular systems for improved targeting and therapeutic outcomes. However, the clear correlation between CMC and in vivo performance has yet to be established.

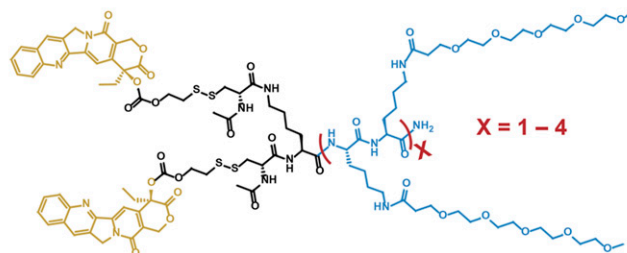
In this article, we report the design and synthesis of four self-assembling prodrugs (SAPDs) of various CMCs that all self-assemble into SPs. The direct use of anticancer drug as molecular building units allows for accurate assessment of CMC influence on their therapeutic efficacy. Our results suggest that the CMC value of a SP has a significant impact on their biodistribution and pharmacological behavior, which is reflected on the maximum tolerated dose (MTD), tumor accumulation, toxicity, and eventually the therapeutic efficacy in suppressing tumor growth.

Results and Discussion

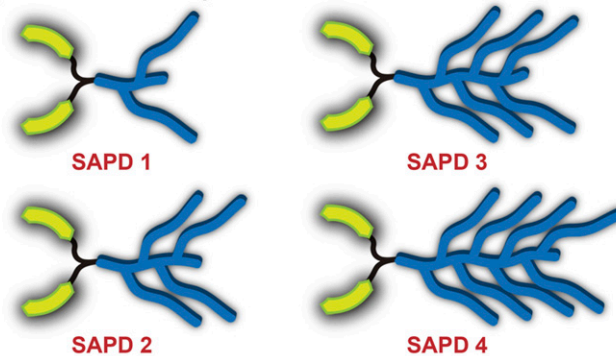
Molecular Design. Fig. 1 shows the molecular design of the four SAPDs studied, comprising two hydrophobic CPT molecules and oligoethylene-glycol (OEG)-decorated peptides of various OEG numbers (2, 4, 6, 8). The design rationale herein is that the CPT moiety, in addition to its pharmacological role, can provide directional, associative π - π interactions to contribute to the self-assembly process. By fixing the number of CPTs and varying the hydrophilicity of peptide segments, we are able to create four SAPDs of different hydrophilic-lipophilic balances (HLBs), leading to formation of SPs of different stability (43, 44). The use of the OEG segment to modify the side chain of lysine endows a nonionic and neutral surface chemistry to the resultant SPs, so as to reduce protein adsorption and increase circulation half-lives (45). In addition, the CPT and the hydrophilic moiety are connected via a biodegradable disulfanyl-ethyl carbonate linker (etcSS), which was shown to effectively release the parent CPT upon contact with intracellular glutathione (GSH) (31, 32, 46–48). The detailed synthetic procedures and characterizations are included in *SI Appendix, section 2 and Figs. S1–S10*. Briefly, the peptide auxiliaries were synthesized using standard 9-fluorenylmethoxycarbonyl (Fmoc) solid-phase peptide synthesis protocols (*SI Appendix, Fig. S1*). The OEG units were grafted onto lysine side chains by amide formation reaction similar to coupling of amino acids. After purification using preparative reversed-phase high-performance liquid chromatography (RP-HPLC), OEG-decorated peptides were reacted with CPT-etcSS-Pyr to yield SAPDs using a previously reported method (33, 46). The final products were again purified using preparative RP-HPLC and characterized using analytical HPLC and mass spectrometry (*SI Appendix, Figs. S7–S10*).

Self-Assembly of SAPDs. To study the self-assembly behavior of the SAPDs, we directly dissolved the lyophilized powders in deionized water at a concentration of 2 mM and neutral pH. After aging overnight, cryogenic transmission electron microscopy (cryo-TEM) imaging (Fig. 2 *A–D*) reveals that all of the SAPDs can self-assemble into one-dimensional (1D) nanostructures.

A Chemical structure of self-assembling prodrugs (SAPDs)



B Cartoon of SAPD platform



C Self-assembly of SAPD into supramolecular polymer (SP)

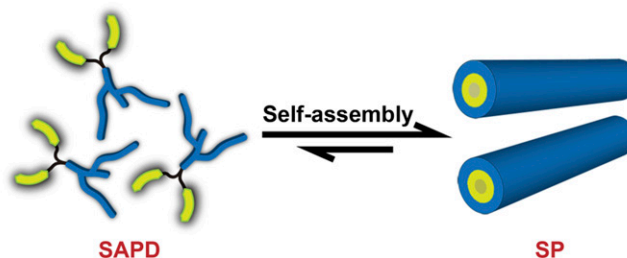


Fig. 1. Schematic illustration of the design and self-assembly of self-assembling prodrugs (SAPDs). (A) Chemical structure of the designed SAPDs. (B) Cartoon of SAPD platform. Two hydrophobic camptothecin (CPT) molecules (yellow) were conjugated with four different oligoethylene-glycol (OEG)-decorated hydrophilic auxiliaries (blue) through the biodegradable etcSS linker (black) to create SAPDs 1 to 4, respectively. (C) Illustration of self-assembly of SAPD into supramolecular polymer (SP).

More specifically, SAPD 1 formed supramolecular filaments of around 9 nm in diameter and several micrometers in length (Fig. 2*A*), and SAPD 2 self-assembled into shorter filaments with a majority less than 400 nm in length (Fig. 2*B*). Conventional TEM images (*SI Appendix, Fig. S12*) clearly reveal the hollowed filaments of assembled SAPDs 1 and 2, a result of highly ordered packing of CPT moieties within the hydrophobic core (25, 49). SAPDs 3 (Fig. 2*C*) and 4 (Fig. 2*D*) both aggregated into micrometer-long nanoribbons of various widths with slight twisting observed. The formation of those 1D assemblies is believed to be a result of strong π - π interactions among CPT units, acting in concert with the intermolecular hydrogen bonding among the OEGlyated peptides. The complex interplay of these two associative interactions promotes the directional growth of the observed SPs and defines the resulting morphology, despite no inclusion of any β -sheeting-forming peptide sequences in the molecular design (1, 43, 44, 50–52). The slight differences in the length and morphologies could be plausibly attributed to the increase of overall HLB values and steric hindrance caused by OEG moieties that weaken the hydrophobic associations, and also the strengthened intermolecular hydrogen bonding capacity

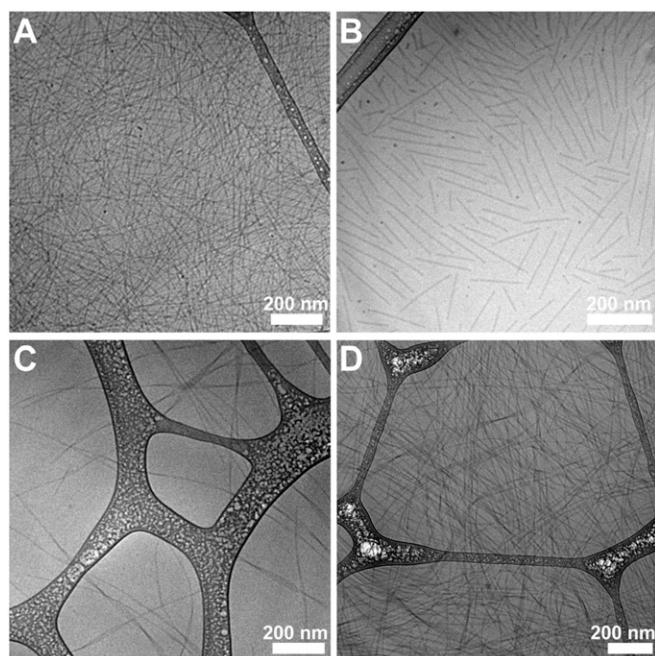


Fig. 2. Supramolecular polymers (SPs) formed by SAPDs in water. Representative cryo-TEM of supramolecular assemblies of SAPD 1 (A), SAPD 2 (B), SAPD 3 (C), and SAPD 4 (D). TEM images reveal that all of the prodrugs self-assembled into 1D structures. All concentrations: 2 mM.

that could shift the directional associations from π - π dominant mode to hydrogen bonding controlled manner. Furthermore, the neutral surface chemistries of the SPs were confirmed by ζ -potential measurement of all four assembled SAPDs in the PBS buffer, showing slightly negative values of -6.5 , -7.4 , -6.5 ,

and -5.9 mV for SAPDs 1 to 4, respectively (SI Appendix, Fig. S11). These results indicate that all SAPDs can assemble into SPs, albeit with slight variations in length and morphology, that are solely made of prodrugs without any external materials or pharmaceutical excipients.

CMC Measurement of SAPDs. We next assessed the CMC values for each of the designed SAPDs in aqueous solution. It is worth mentioning that for peptide-based amphiphiles it is not uncommon that the CMC values differ from their critical assembly concentration (CAC). Velichko et al. (53) revealed in a simulation study that peptide amphiphiles with a strong hydrogen bonding sequences could first assemble into β -sheets before micellization into well-defined supramolecular nanofibers with a hydrophobic compartment. Experimentally, the CAC is often measured using spectrometry techniques such as circular dichroism (CD) to reveal the presence of intermolecular associations and packing at a much lower concentration. In the case reported here, the CMC values were measured in the PBS buffer using Nile Red as a probe, which fluoresces intensely in hydrophobic environments and is strongly quenched and red-shifted in aqueous media (54, 55). Measuring fluorescent spectra excited at 550 nm of SAPD solutions of varying concentrations, and then plotting the ratio of intensity at 635 nm (emission maximum of the Nile Red in hydrophobic environment) to that at 660 nm (emission maximum in aqueous conditions) against the concentration of SAPDs, yielded the plots shown in Fig. 3A. According to the changes in fluorescence intensity, the CMC values are estimated to be 2.7 and 10.1 μ M for SAPDs 1 and 2, respectively. The CMCs of SAPDs 3 and 4 exceed 200 μ M and cannot be accurately extracted. The CMC experiments suggest that structural stability of the SAPD SPs would be SAPD 1 > SAPD 2 > SAPDs 3 and 4 and that SAPDs 3 and 4 are unable to form stable assemblies at the concentration of submillimolar range.

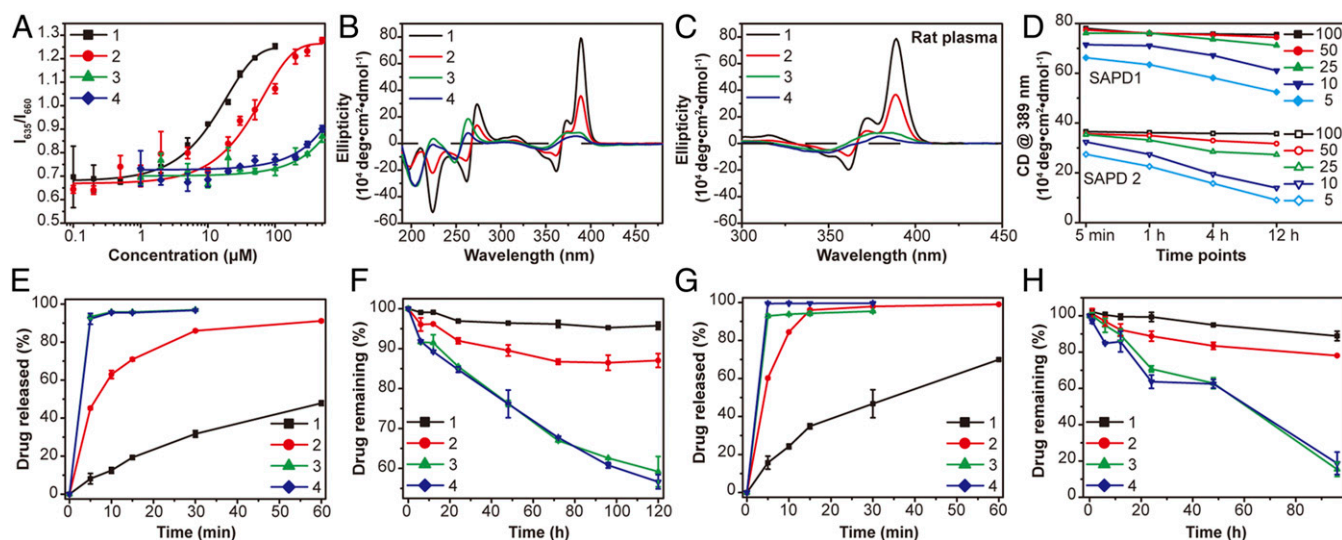


Fig. 3. CMC, stability, and drug release studies of SAPDs. (A) CMC measurement of SAPDs using a Nile Red method. CMCs of SAPDs 1 and 2 are estimated to be 2.7 and 10.1 μ M, respectively. CMCs of SAPDs 3 and 4 exceed 200 μ M, and the exact values cannot be directly determined here. (B) CD spectra of SAPDs at 200 μ M in water. SAPD 1 shows very strong absorptions attributed to CPT chromophore interactions and intermolecular hydrogen bonding. SAPD 2 shows a similar pattern with largely reduced intensities. The lack of typical hydrogen-bonding interactions and characteristic CPT absorptions in SAPDs 3 and 4 indicates that they may not form 1D nanostructures at the concentration of 200 μ M. The chromophore absorptions can be ascribed to intramolecular CPT interactions within a single prodrug. (C) CD spectra of SAPDs at 200 μ M in 10% rat plasma. No apparent difference in the absorptions of SAPDs 1 and 2 were observed compared with those in water, while slight changes can be seen in the cases of SAPDs 3 and 4. (D) Plots of absorption of SAPD 1 and SAPD 2 assemblies at 389 nm in the time- and concentration-dependent CD measurement. Drug release plots of SAPDs at 200 μ M in PBS (E) and rat plasma (G) with 10 mM GSH. Cumulative drug degradation plots of SAPDs at 200 μ M in PBS (F) and rat plasma (H) without GSH. $n = 3$ for all drug release studies.

Molecular Packing of SAPD Monomeric Units in the SPs. To further validate our hypothesis that the increase of OEG repeat numbers in peptides would decrease the supramolecular stability of the resulting SPs, we performed CD spectroscopy measurements to understand the molecular arrangement within the SPs at the concentration of 200 μM (Fig. 3B). CD spectrum of assembled SAPD 1 shows two bisignate signals centered at 266 and 367 nm, and a strong positive signal at 389 nm, suggesting the highly ordered internal packing of CPT molecules (25, 56). The negative peak around 223 nm corresponds to hydrogen-bonding interactions among the peptide segments (57, 58). SAPD 2 solution presents similar CD pattern to that of SAPD 1, but with significantly decreased intensity, revealing that these two building units have similar interior molecular packing (Fig. 3B). The lower intensity of SAPD 2 can be probably attributed to a looser CPT packing as a result of increased hydrophilic–lipophilic ratio and steric repulsive force posed within the peptide auxiliaries that weakens the π – π stacking among CPT units. These findings are also consistent with TEM results (Fig. 2 A and B and *SI Appendix*, Fig. S12) that both SAPD 1 and 2 form filamentous assemblies, but the length of assembled SAPD 1 is much longer than that of SAPD 2. The CD spectra of SAPDs 3 and 4 both show a small hump between 350 and 400 nm, a blue-shifted bisignate signal at 256 nm, and a negative peak around 204 nm, which are drastically different from those of SAPDs 1 and 2 (Fig. 3B). The lack of typical hydrogen-bonding absorption indicates that SAPDs 3 and 4 may not be able to form any stable SPs at this studied concentration (200 μM), and the chromophore absorptions could be possibly attributed to intramolecular CPT association within an individual prodrug, along with some loose intermolecular associations. These observations suggest that the number of OEG repeat units is critical for the formation of stable SPs, and the increased OEG chains would raise the concentration threshold for directional supramolecular growth of SAPD monomers.

Stability of SAPDs in Protein Environments. The interactions of nanoparticles with serum proteins are known to impact the disassociation of supramolecular assemblies in biologically relevant environment. For example, Talmon and coworkers (59) have reported the disassociation of multilamellar lipoplexes in the presence of serum via cryo-TEM. To assess the stability of assembled SAPDs in more complex biological media, we performed CD experiments to investigate their long-term stability in various serum environments. SAPD solutions (2 mM) were diluted using rat plasma (Fig. 3C), FBS (*SI Appendix*, Fig. S13A), and mice plasma (*SI Appendix*, Fig. S13B) to yield a final concentration of 200 μM , which were then aged overnight before CD measurement was taken. We found no noticeable changes in the absorptions of SAPDs 1 and 2 in the protein environments (Fig. 3C and *SI Appendix*, Fig. S13) compared with those in aqueous solution (Fig. 3B), while some slight changes can be observed for SAPDs 3 and 4. These results show that serum proteins had limited impact on the stability of SAPD 1 and 2 assemblies, but could be a factor destabilizing the assemblies of SAPDs 3 and 4. We also performed experiments to assess their kinetic stability upon plasma dilution, mimicking the dissociation process of SPs after i.v. injection. Solutions of SAPDs 1 and 2 (2 mM) were diluted to 100, 50, 25, 10, and 5 μM in rat plasma, and time-dependent CD spectra were recorded at 5 min, 1 h, 4 h, and 12 h (*SI Appendix*, Fig. S14). By monitoring the absorption intensity at 389 nm (Fig. 3D), we found that SAPD 1 is highly stable upon dilution over time at concentrations above 25 μM . However, at 10 and 5 μM , the absorption at 5 min was observed to drop by 10% and 15%, respectively. At 12 h, the decrease reached 22% and 33%, respectively. SAPD 2 demonstrated a similar trend but showed a higher propensity to dissociate as a result of its higher CMC value. These results suggest that the SAPD assemblies

tend to disassociate upon dilution, and the dissociation became apparent when the concentration of the diluted solutions drops near their CMCs.

In Vitro Drug Release Assessment of SAPDs in Physiological Environments. We next discovered that the four SPs possess very different in vitro drug release profiles in both PBS buffer and rat plasma. In these experiments, we first prepared a series of sample solutions to investigate the drug release of four SAPDs at the concentration of 200 μM in PBS buffer at 37 $^{\circ}\text{C}$ with or without 10 mM GSH, respectively (Fig. 3 E and F and *SI Appendix*, Figs. S15 and S16). Fig. 3E shows the summary of drug release of SAPDs over 60 min in the presence of GSH, and *SI Appendix*, Fig. S15A exhibits the representative analytical RP-HPLC traces of drug release in GSH environment at 5 min. Clearly, the drug release rate is SAPD 1 < SAPD 2 < SAPDs 3 and 4, with 8% of SAPD 1, 45% of SAPD 2, 93% of SAPD 3, and 92% of SAPD 4 degraded within 5 min (Fig. 3E and *SI Appendix*, Fig. S15A), evidently demonstrating that more stable SPs show increased resistance to GSH-relevant cleavage compared with the less stable ones. It is highly plausible that SAPDs in the assembled state could shield the hydrophobic CPTs and biodegradable linkers from the external environment and thus hinder the liberation of drugs. At this studied concentration, more SAPD 1 exists in the SP form than SAPD 2, while SAPDs 3 and 4 mostly exist in the monomeric forms, thus showing little resistance to GSH. Fig. 3F presents the chemical degradation profile of SAPDs over 120 h in the absence of GSH, with the representative analytical RP-HPLC traces included in *SI Appendix*, Fig. S15B. In the absence of GSH, hydrolysis of the carbonate ester linker is considered to be mainly responsible for the prodrug degradation. Similar to the findings in the GSH environment, SAPD 1 exhibits the most resistance toward hydrolytic cleavage with 96% of conjugates remaining intact, compared to 87% of SAPD 2 and less than 60% of SAPDs 3 and 4 after 120-h incubation (Fig. 3F and *SI Appendix*, Fig. S16). We also repeated this drug release experiment in rat plasma containing a myriad of proteins and enzymes (Fig. 3 G and H). The same drug release trend of SAPD 1 < SAPD 2 < SAPDs 3 and 4 was observed, albeit with slightly faster drug release rates relative to those in PBS, likely caused by protein-promoted dissociation and enzyme-induced degradation. The percentages of SAPDs 1 to 4 of remaining drugs in plasma at 96 h without GSH are 89%, 78%, 15%, and 18% (Fig. 3H), respectively, in comparison to 95%, 86%, 63%, and 61% in PBS (Fig. 3F). Altogether, these results clearly suggest that SPs with a lower CMC value are more resistant to disassemble and liberate the free drugs in physiological environments.

Dose–Response Inhibition against Colon Cancer Cells. As a result of the effective release of potent CPT in a GSH-rich environment, all SAPDs were found to demonstrate great efficacy against cancer cells. The in vitro cytotoxicities of SAPDs were evaluated against HT-29 and HCT-116 human colorectal cancer cells through a dose–response relationship assay based on CPT concentration using the sulforhodamine B method. SAPDs of various concentrations were incubated with cancer cells for 72 h with both free CPT and irinotecan, a clinically used prodrug of CPT for treatment of colorectal cancer, as controls (Fig. 4). All of the prodrugs exhibited a higher potency against cancer cells compared with irinotecan, which must be hydrolyzed prior to exerting its therapeutic efficacy (60). Although showing slight variations, the IC_{50} values of SAPDs are within similar ranges, which are two orders of magnitude lower than that of irinotecan in both cell lines. These results led us to conclude that the design of GSH-responsive etcSS linker enables SAPDs to undergo a rapid GSH-induced restoration of potent free CPT that is much faster than hydrolysis of irinotecan, and the differences in CMC

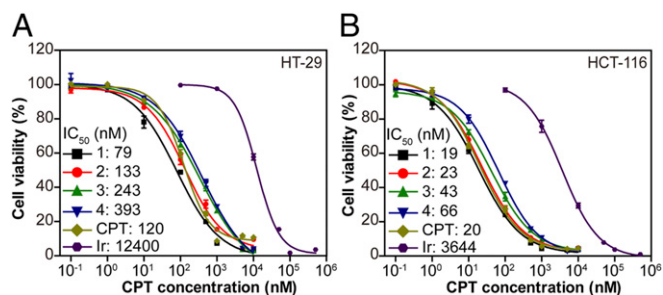


Fig. 4. In vitro cell cytotoxicity of SAPDs against HT-29 colorectal adenocarcinoma cells (A) and HCT-116 colorectal carcinoma cells (B), with both free CPT and irinotecan as controls (72-h incubation, $n = 3$).

values and the related free drug release rate are not reflected on their in vitro efficacy against cancer cells.

Antitumor Performance of SAPDs of Various CMCs at the Same Dose.

To better understand the role of CMC in its in vivo performance, we next assessed antitumor effect of SAPDs of various CMCs in a HT-29 mouse xenograft model through i.v. administration of four prodrugs at a dose of 10 mg/kg (CPT equivalent) on days 1, 5, 9, and 13 ($n = 6$ for each group) with PBS ($n = 5$) and free CPT (9 mg/kg, $n = 5$) as controls. Hydrophobic free CPT was dissolved in a mixture of DMSO/ethanol/PEG-400/water at a volumetric ratio of 1:1:2:1 and administrated through intraperitoneal (i.p.) injection to minimize the toxicity of organic solvents (61). Although i.p. injection of organic solvent is tolerable, administration of free CPT at 9 mg/kg still resulted in the death of all five mice after the

second dose due to the associated severe toxicity of the free CPT drug (Fig. 5C). In addition, irinotecan ($n = 5$) at its reported MTD of 100 mg/kg was also intraperitoneally injected on days 1, 8, and 15 as another control (61). Significant tumor regression (Fig. 5A) with much improved survival (Fig. 5C) was observed in mice treated with all SAPDs compared with the control group. SAPD 1 showed the best tumor suppression activity with a mean tumor volume of 60 mm³ on day 25 compared with 255, 304, 286, and 194 mm³ for SAPDs 2 to 4 and irinotecan, respectively (Fig. 5A). Also, the administration of SAPD 1 increased the median survival from 27 d (the control group) to 56 d, while the median survivals of other groups were 46 d (SAPD 2), 42 d (SAPD 3), 47 d (SAPD 4), and 51 d (irinotecan), respectively. These results suggest that the most stable SPs assembled from SAPD 1 exhibited the best efficacy compared with other SAPDs when administrated at the same dose. One possible explanation could be that less stable SPs may dissociate into more monomeric forms of the prodrugs upon plasma dilution, which is subject to a rapid renal clearance. Importantly, one could notice that SAPD 1 generated the most toxicity according to the body weight change, although it is within acceptable toxicity range (Fig. 5B).

In Vivo Circulation Study of SAPDs. To provide more insight into the circulation fate of SAPD assemblies in vivo, we collected the pharmacokinetic profiles of the four SAPD SPs in Sprague-Dawley (SD) rats ($n = 3$ for each prodrug) through i.v. injection at the dose of 10 mg/kg (CPT equivalent). The initial concentration of SAPDs upon plasma dilution is roughly estimated to be around 150 μ M (SI Appendix), a value above the CMCs of SAPDs 1 and 2 but below those of SAPDs 3 and 4. We found that the SAPD 1 group showed the slowest clearance of drugs from the plasma, followed by SAPD 2, SAPD 3, and SAPD 4. As

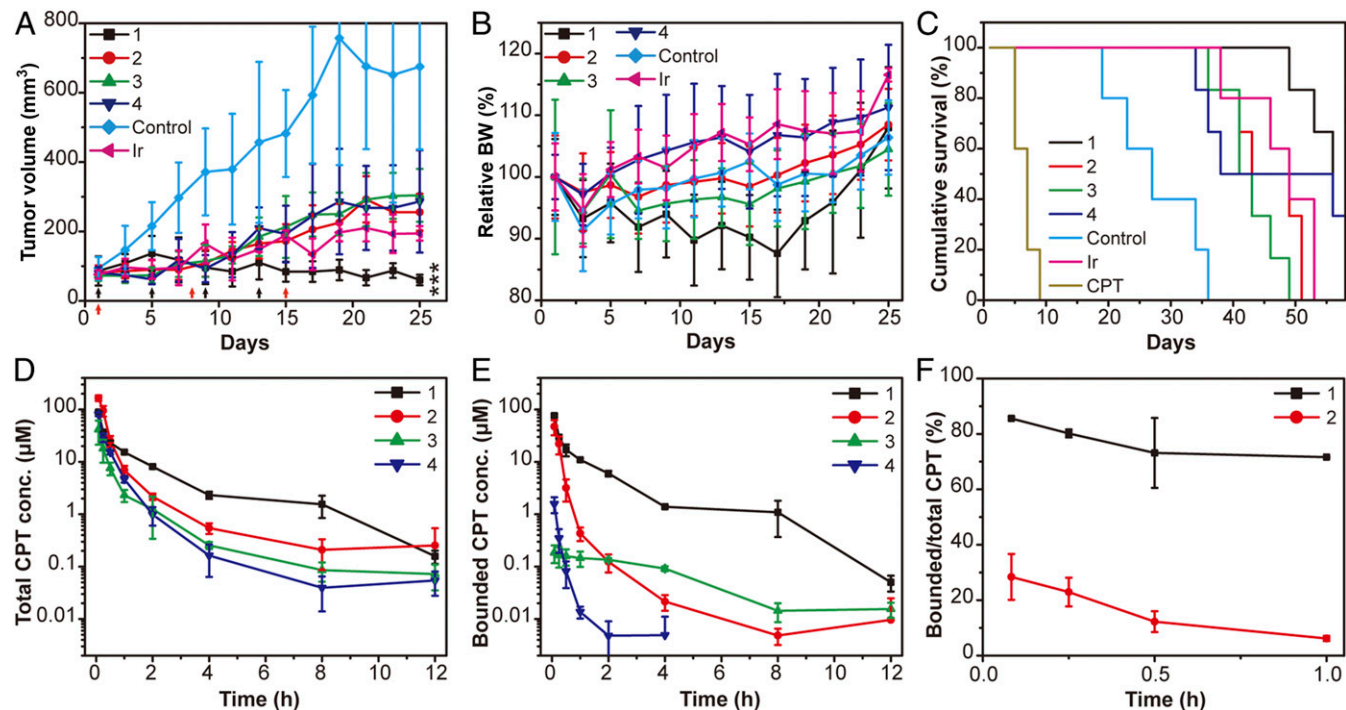


Fig. 5. In vivo antitumor efficacy and circulation study of SAPDs at the same dose (10 mg/kg, CPT equivalent). SAPDs were i.v. injected q4dx4 (black arrows) at days 1, 5, 9, and 13 at a dose of 10 mg/kg mice ($n = 6$). Blank PBS group and free CPT (i.p.) at a dose of 9 mg/kg (q4dx4) at days 1, 5, 9, and 13 were taken as controls ($n = 5$); however, administration of CPT resulted in death of all five mice after the second dose. Irinotecan (i.p.) at a dose of 100 mg/kg (qwx3, red arrows) at days 1, 8, and 15 was another control ($n = 5$). Tumor volume (A), body weight (B), and cumulative survival (C) plots of mice. Loss of mice is a result of treatment-related death or killing after predetermined end point was reached. All of the data are presented as mean \pm SD and analyzed by one-way ANOVA (Fisher; $0.01 < *P \leq 0.05$; $**P \leq 0.01$; $***P \leq 0.001$). Real-time concentration of total CPT (D) and bounded CPT in SAPDs (E) in the circulation study on SD rats ($n = 3$) at 5 min, 15 min, 30 min, 1 h, 2 h, 4 h, 8 h, and 12 h. (F) The ratio of bounded CPT in SAPDs to total CPT within 1 h after injection.

shown in Fig. 5D, the total CPT concentrations for SAPDs 1 to 4 are 15.3, 7.0, 2.8, and 4.7 μM at 1 h, and 8.1, 2.2, 1.3, and 1.0 μM at 2 h, respectively. More importantly, SAPD 1 maintained the lowest degradation in plasma (Fig. 5E), with 86% of CPT remained in the bounded form at 5 min in comparison to only 28% for SAPD 2 (Fig. 5F). Even at 1 h, more than 72% of total CPT retained the conjugate form (Fig. 5 E and F). In sharp contrast, both SAPD 3 and SAPD 4 rapidly broke down into free CPT upon injection, with more than 98% CPT released within 5 min (Fig. 5 D and F and *SI Appendix*, Fig. S17), suggesting that after i.v. injection their assemblies quickly dissociate into monomeric form upon plasma dilution and that their unassembled forms are vulnerable to in vivo enzymatic/hydrolytic degradation. These results are consistent with our in vitro studies, further supporting the notion that CMCs represent an important characteristic to determine the morphological and structural integrity of supramolecular assemblies during circulation.

Systemic Toxicity and MTD Determination of SAPDs. Given that the therapeutic index of a drug is determined by both systemic toxicity and therapeutic efficacy, it is important to investigate the role of CMC of a SP in its systemic toxicity. We then studied the MTD of SAPDs by a dose escalation study in healthy female athymic nude mice (Table 1 and *SI Appendix*, Table S1), which is defined by the largest dose given to a rodent that did not result in more than a 20% body weight loss or death. We found that SAPDs 1 to 4 have MTDs of 24, 54, 72, and 72 mg/kg, respectively (49). The MTD trend of SAPD 1 < SAPD 2 < SAPD 3 and SAPD 4 (Table 1 and *SI Appendix*, Table S1), along with body weight fluctuation in the above-mentioned efficacy study (Fig. 5B), led us to draw the conclusion that the lower the CMC of a SP, the lower its MTD and the higher the drug's systemic toxicity. The decrease of MTD upon using stable nanostructures as drug carriers was also reported in the design of liposomal irinotecan (62–65). Previous studies have shown that encapsulation of irinotecan into liposomes showed higher toxicity than the free irinotecan in tumor-free SCID/Rag-2M mice and administration of irinotecan-encapsulated liposome at the MTD of

free irinotecan resulted in significant body weight loss of studied mice (62). In addition, the MTD of ONIVYDE monotherapy at 3-wk interval was reported as 120 mg/m² in clinic compared with that of 320 mg/m² for irinotecan (63–65). The corroboration of our findings with these reports suggest that it is likely that small-molecule drugs can undergo a rapid clearance from the body that largely reduces their bioavailability. The liposomal formulation protects the drugs within stable nanostructures, which could improve the circulation, but at the same time increase the drugs' accumulation in healthy organs. Therefore, we speculate that SAPD assemblies in more stable forms enable a longer retention time by reducing its body clearance, which could result in higher uptake by the major organs and thus the higher toxicity at the same dose level.

Antitumor Performance of SAPDs at Their Respective MTDs. Given that SAPDs 1 to 4 showed excellent tolerability in the above-mentioned efficacy study (Fig. 5) and that intensification of dosage to improve treatment outcome is often favored within a drug's tolerability, we decided to elevate the dose to assess whether a better tumor inhibition efficacy can be achieved. Based on our previous experiences, the MTD of multiple injections (three doses and 4 d a dose) could be around one-half of the MTD of a single injection (Table 1 and *SI Appendix*, Table S1). For example, the MTD of SAPD 1 of multiple injections is 12 mg/kg, which is one-half of the MTD (24 mg/kg) of a single injection (49). Thus, in the following efficacy study, we used the dose of one-half MTD for each prodrug, which is 12 mg/kg (one-half MTD) for SAPD 1 and 36 mg/kg for both SAPD 3 and 4, respectively. Regardless of a slightly lower MTD (54 mg/kg) of SAPD 2 compared with that of SAPDs 3 and 4 (72 mg/kg), we decided to use 36 mg/kg for consistency; the irinotecan group and PBS group were also used as controls (Fig. 6). Again, all of the SAPDs significantly suppressed the tumor growth at the dose of their estimated MTDs relative to the control group (Fig. 6A). The treated mice showed a mean tumor volume of 172, 330, 322, 408, and 358 mm³ for SAPDs 1 to 4 and irinotecan, respectively, on day 28 (Fig. 6A). SAPD 1 was a bit more effective than other SAPDs; however, it is not statistically significant as analyzed by one-way ANOVA ($P > 0.05$), except relative to SAPD 4 ($P = 0.02$). Furthermore, SAPD 2 showed systemic toxicity with one treatment-related death (Fig. 6C), which also indicates that the predetermined dose could be higher than the MTD of SAPD 2. A similar trend was observed in survival, in which SAPD 1 slightly improved the survival of mice compared with the other groups. Although we cannot rule out that further increase of the dose of SAPDs 2 to 4 would lead to an even better efficacy (it may also lead to more severe toxicity), our current results suggest that the efficacy of SAPDs 2 to 4 does not exceed SAPD 1 even at their respective estimated MTDs.

These in vivo experimental results collectively demonstrate the significant role of CMC values in determining the circulation, therapeutic efficacies, and systemic toxicities of SPs. Scheme 1 illustrates the possible four destinations that therapeutic SPs could reach after systemic administration, which are closely related to their circulation, efficacy, and toxicity. Following i.v. injection, SPs could be contained within plasma (circulation), accumulate in tumorous tissues (efficacy) or healthy organs (toxicity), or get cleared out through the excretion systems. As a result of their supramolecular nature, all SAPD SPs are expected to undergo spontaneous dissociation after plasma dilution into fragmented pieces and monomeric units (66). From the perspective of pharmacokinetics, smaller fragments (<6 nm) and monomeric prodrugs can be rapidly excreted through the renal system (Scheme 1). This explains why SAPDs 2 to 4 had a higher respective MTD than SAPD 1 because more of their monomers were likely excreted out of the studied mice. Since fewer SAPDs 2 to 4 are left within the body, it consequently lowered the accumulation in both tumor and healthy tissues, thus leading to reduced treatment efficacy and increased MTD. In contrast, a larger percentage of SAPD 1 is expected to assume the supramolecular form during the

Table 1. MTD of SAPDs 2 to 4 by dose escalation studies in healthy athymic nude mice

Prodrug	Dose, mg/kg	Maximum % BW loss, d	Survival/total
SAPD 2	108	N.D.	0/3
	72	11.4 (2)	2/3
	54	3.5 (2)	3/3
	45	4.0 (2)	3/3
	36	2.1 (6)	3/3
	18	6.2 (5)	3/3
SAPD 3	108	N.D.	2/3
	72	0	3/3
	54	1.6 (1)	3/3
	45	2.5 (4)	3/3
	36	1.4 (4)	3/3
	18	5.5 (4)	3/3
SAPD 4	108	N.D.	1/3
	72	1.2 (1)	2/3
	54	3.9 (3)	3/3
	45	0	3/3
	36	7.2 (2)	3/3
	18	3.1 (5)	3/3

A single i.v. injection of SAPDs was administered, and body weights (BW) of mice were recorded for 2 wk ($n = 3$ for each group). All of the doses are CPT equivalent. The MTD of SAPD 1 was previously determined in our laboratory (*SI Appendix*, Table S1). SAPDs 1 to 4 have MTDs of 24, 54, 72, and 72 mg/kg, respectively. If the BW of a mouse decreases more than 20%, the mouse will be killed and counted as a death.

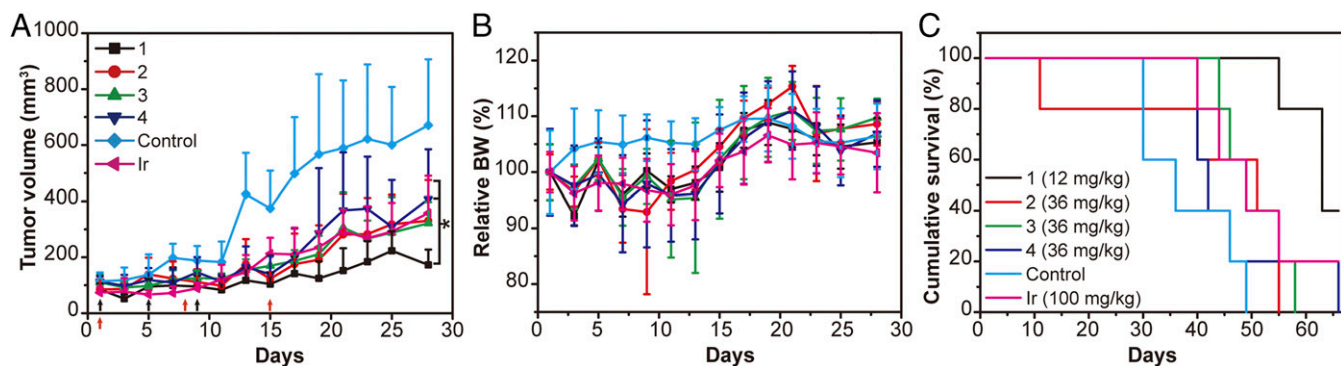


Fig. 6. In vivo antitumor efficacy of SAPDs at their respective estimated MTDs. SAPDs were i.v. injected q4dx3 (black arrows) on days 1, 5, and 9 at doses of 12 mg/kg (CPT equivalent) for SAPD 1, and 36 mg/kg for all other three SAPDs ($n = 5$). Blank PBS group ($n = 5$) was taken as a control, and irinotecan (i.p.) at a dose of 100 mg/kg (qwx3, red arrows) on days 1, 8, and 15 was another control ($n = 5$). Tumor volume (A), body weight (B), and cumulative survival (C) plots of mice. Slight decrease of body weight was observed in all treated groups with one treatment-related death in the SAPD 2 group. All of the data are presented as mean \pm SD and analyzed by one-way ANOVA (Fisher; $0.01 < *P \leq 0.05$; $**P \leq 0.01$; $***P \leq 0.001$).

circulation, which is too big for renal clearance, so as to improve accumulation in tumors for better treatment efficacy. Although SAPD 2 has a CMC value (10.1 μ M) close to that of SAPD 1 (2.7 μ M) and behaved similarly in their in vitro stability under the quiescent conditions (Fig. 3 C and D) and prodrug release in the absence of GSH (Fig. 3 F and H), SAPD 2 filaments were observed to rapidly dissociate into monomeric units after i.v. administration (Fig. 5E). As a result, SAPD 2 demonstrated a much higher MTD (54 vs. 24 mg/kg) and a much reduced efficacy in tumor suppression. These observations suggest that the CMCs, in vitro stability, and drug release data measured under quiescent conditions only provide qualitative information to predict the drug's in vivo performance. It is the drug's in vivo stability and pharmacokinetic profile that afford more reliable prediction of its in vivo efficacy.

On basis of our in vivo study results, SAPD 1 appears to be the best candidate for further development as it revealed the best efficacy in suppressing tumor growth at the same dosage (10 mg/kg), and also a comparable efficacy even when SAPDs 2 to 4 were administered at their respective MTD. However, it should be noted that, although SAPD 1 demonstrated the best in vivo efficacy, it also revealed the greatest toxicity by having the lowest MTD. Thus, an optimal CMC value should exist to balance the healthy organ toxicity with the tumor treatment efficacy. This statement also eludes that permanent locking of supramolecular nanostructures through shell or internal cross-linking may not

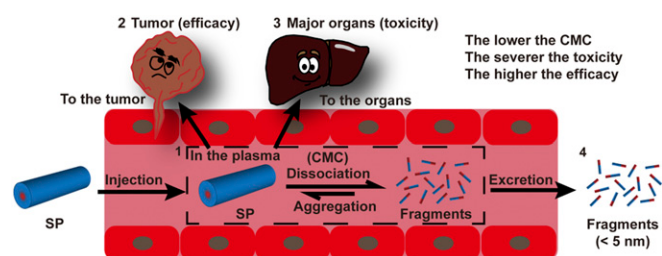
represent the best strategy as it would also boost toxicity to healthy organs, and also highlights the important role that supramolecular assemblies could play in the development of more effective drug carriers. In drug development, therapeutic index is an important measure of therapeutic efficacy relative to the toxicity it may cause. A higher therapeutic index is often preferred as it suggests a favorable safety and efficacy profile. In our case, although we cannot directly assess the therapeutic index for each SAPD design, we can envision an improved therapeutic index for all of the studied SAPDs over the parent drug CPT. Our studies also reveal the tunability of therapeutic index through molecular engineering of SAPDs, given their difference in MTD and treatment efficacy.

Conclusion

In this article, we developed a series of SAPDs to achieve a better understanding of the fundamental role of CMC of SPs in their in vivo efficacy in tumor inhibition and systemic toxicity. Our results provided a general guiding principle in design of SPs from two important perspectives: 1) antitumor efficacy and 2) toxicity. The antitumor efficacy is largely dependent upon the stability of the SPs, which allows for reduced clearance and thus improved accumulation in tumor sites. At the same time, the toxicity is more closely related to the monomer clearance, with less stable SPs having a higher MTD. Our results suggested that lowering the CMC value would lead to increased toxicity (body weight loss) yet improved efficacy in tumor suppression in rodents. Although we cannot rule out the potential impact of the morphology and length, our studies identified the primary design principles of self-assembling building units and the essential roles of supramolecular integrity in altering therapeutic index of SPs. We hope that these findings will contribute to the eventual elucidation of supramolecular drug delivery systems and lead to successful design of clinically usable SPs.

Materials and Methods

Detailed synthesis and experimental protocols, in addition to *SI Appendix*, Figs. S1–S17 and Table S1, can be found in *SI Appendix*.



Scheme 1. Illustration of the circulation fate of a supramolecular polymer (SP) after entering into the circulation. SP (1) may dissociate into fragments/monomers in the plasma upon dilution, and the dissociation kinetics is mostly dictated by its CMC. SP has the tendency to accumulate more in the tumor (2) and major organs (3) (liver, spleen, kidney, lung, and heart), while fragments/monomers (4) tend to undergo a rapid renal clearance. Thus, the lower the CMC of a SP, the lower the percentage of fragments and monomers, leading to reduced excretion and enhanced tumor (improved efficacy) and healthy organ uptake (increased toxicity).

CMC Measurement. Nile Red method was used to investigate the CMCs of four SAPDs by taking advantage of its unique fluorescent behavior in the hydrophobic environments (54, 55). Once the concentration exceeds CMC, Nile Red could associate with hydrophobic domain within the assemblies and emit strong fluorescence. A stock solution of Nile Red at the concentration of 500 μ M was prepared in acetone. Then 10 μ L of the prepared stock solution was added to microcentrifuge tubes, which was allowed to evaporate the acetone in the dark. The 500- μ L SAPD solutions of various concentrations were added into those microcentrifuge tubes and allowed to age overnight.

The emission spectra from 580 to 720 nm were acquired on a Fluorolog spectrofluorometer (Horiba Jobin Yvon) with an excitation wavelength of 550 nm. The ratios of intensity at 635 nm (emission maximum in hydrophobic environment) to that at 660 nm (emission maximum in aqueous conditions) of various solutions were calculated and plotted against the concentrations.

CD Measurement of SAPDs in Physiological Environments. Stock solutions of SAPDs were prepared at 2 mM and aged overnight. The solutions were diluted to 200 μ M in 10% FBS, 10% mice plasma, and 10% rat plasma, aged overnight before CD measurement. To study the kinetic stability of the assembled SAPDs upon dilution, the stock solutions of SAPDs 1 and 2 were diluted to 100, 50, 25, 10, and 5 μ M in 10% rat plasma. The CD spectra were recorded at 5 min, 1 h, 4 h, and 12 h. All of the CD spectra were recorded from 300 to 450 nm using a 1-mm path length quartz cell. The spectra were collected and normalized from ellipticity (millidegrees) to molar ellipticity (degree-centimeter squared per decimole).

Drug Release and Chemical Stability Studies of SAPDs. Drug release studies of four SAPDs were performed at a concentration of 200 μ M in PBS buffer with or without the reducing agent GSH. Briefly, 400 μ M stock solutions of SAPDs in water were prepared and aged overnight. Stock solutions containing 2 \times PBS (20 mM) with or without 20 mM GSH were prepared 1 h before the experiment, and the pH was tuned to 7.4 with NaOH. The prodrug solutions were further diluted to 200 μ M with 20 mM (2 \times) PBS buffer with or without GSH (20 mM) to give final solutions of 200 μ M prodrug, 10 mM PBS, and with or without 10 mM GSH. Three replicates of each SAPD were prepared with or without GSH and were incubated at 37 $^{\circ}$ C. Samples with GSH were collected at 0 min, 5 min, 10 min, 15 min, 30 min, 1 h, and 2 h, while samples without GSH were collected at 0, 6, 12, 24, 48, 72, 96, and 120 h. To prevent further reaction after sample collection, the collected samples (50 μ L each point) were acidified by adding 0.2 μ L of 2 M HCl, frozen with liquid nitrogen, and stored at -30 $^{\circ}$ C. The release profile was determined by analytical RP-HPLC using the following conditions: Varian Pursuit XRs C₁₈ (5 μ m, 150 \times 4.6 mm); 362-nm detection wavelength; 1 mL/min flow rate; the gradient began at 15 to 85% acetonitrile containing 0.1% TFA by 15 min and back to initial gradient at 18 min. The calculated data points were plotted as a percentage of the total CPT concentration against time. Representative HPLC traces over time were also integrated for comparison.

The drug release in rat plasma (10% [vol/vol]) were performed using similar protocols as those in PBS. To determine the amount of SAPDs and free CPT in each sample, 50 μ L of sample was mixed with 200 μ L of acetonitrile (containing 0.1% TFA) and sonicated for 1 min. The supernatants were collected using centrifugation. All samples were filtered through a 0.22- μ m membrane before analysis by an ultraperformance liquid chromatography (UPLC) system (Waters ACQuityTM Ultra Performance LO) equipped with a reverse-phase column (ACQuity UPLC@BEH, C₁₈, 1.7 μ m, 2.1 \times 150 mm) and a fluorescence detector (ACQuity FLR; excitation/emission = 362/430 nm). The column was flushed with a mixture of water (0.1% TFA) and acetonitrile (0.1% TFA) at 0.3 mL/min with the following gradient: 5% acetonitrile (0 to 1 min), 5 to 95% acetonitrile (1 to 5 min), 95% acetonitrile (5 to 8 min), 95 to 5% acetonitrile (8 to 9 min), and 5% acetonitrile (9 to 10 min). Peaks of SAPDs and free CPT were monitored and recorded, and the concentrations were calculated by comparing with standard curves.

Antitumor Efficacy Study of SAPDs at the Same Dose on a HT-29 Tumor Model. HT-29 tumor model was established by s.c. injection of 5 \times 10⁶ HT-29 cells into the right shoulder of female athymic nude mice (8 to 9 wk old). When the averaged tumor size reached 75 to 95 mm³, mice were randomly divided into six groups. Four different SAPDs were all i.v. dosed at 10 mg/kg (CPT equivalent) at days 1, 5, 9, and 13 (n = 6 for each group) with PBS (n = 5), free CPT (n = 5, i.p. injection, 9 mg/kg at days 1, 5, 9, and 13), and irinotecan (n = 5, i.p. injection, 100 mg/kg at days 1, 8, and 15) as controls. Hydrophobic

CPT was dissolved in a mixture of DMSO/ethanol/PEG-400/water at a volumetric ratio of 1:1:2:1 and administered through i.p. injection with a total volume of 100 μ L to minimize the toxicity of organic solvent (61). Based on our experience, i.v. injection of 100 μ L of organic solvent will result in immediate death of the studied mice as a result of solvent-related toxicity, but i.p. injection of 100 μ L of solvent is tolerable. Here, the dose of irinotecan is its MTD as reported in the literature, and i.p. injection achieved similar efficacy to i.v. injection while reducing the side effects (61). The dosing volumes of SAPDs and irinotecan were estimated by a ratio of 200 μ L for a 20-g mouse. The tumor volumes and body weights were monitored and recorded every 2 or 3 d. The tumor volume was estimated by measuring the length and width with calipers and using the equation "tumor volume = (length \times width²)/2." Mice were killed once the tumor volume reached 1,000 mm³.

Circulation Studies of SAPDs in Rats. Female SD rats (200 to 250 g) were randomly grouped into four groups with three rats in each group. SAPDs were all i.v. dosed at 10 mg/kg (CPT equivalent). The dosing volumes of SAPDs were estimated by a ratio of 1 mL for a 200-g rat. The blood samples were collected at 5 min, 15 min, 30 min, 1 h, 2 h, 4 h, 8 h, and 12 h, which were immediately centrifuged to take plasma for further analysis and stored at -80 $^{\circ}$ C. The plasma proteins were precipitated using similar protocols as mentioned above in drug release section and the determination of SAPDs and free CPT in the plasma by UPLC also used the same conditions.

MTD Studies. MTD of SAPD 1 has been previously determined in our laboratory (*SI Appendix, Table S1*). MTDs of other SAPDs were determined by dose escalation studies in healthy female athymic nude mice (Charles River; 12 to 13 wk old). A single i.v. injection of SAPD was dosed at day 1, and the body weights of each mouse (n = 3) were recorded every day for 6 d and every the other day until 2 wk. The dosing volume was determined based upon a ratio of 200 μ L for a 20-g mouse. Doses of SAPDs used in the studied were 108, 72, 54, 45, 36, and 18 mg/kg (CPT equivalent). The MTD was determined by the largest dose that did not result in more than a 20% body weight loss or death of an animal.

Antitumor Efficacy Study of SAPDs at near MTD on a HT-29 Tumor Model. HT-29 tumor model was established as described above. When the averaged tumor size reached 70 to 110 mm³, mice were randomly divided into six groups (n = 5 for each group). Four different SAPDs were all i.v. dosed at near or slightly lower than their estimated MTDs. According to our experience, the MTD of multiple injections (three doses and 4 d a dose) could be around one-half of the MTD of a single injection (Table 1 and *SI Appendix, Table S1*). For example, MTD of SAPD 1 of multiple injections is 12 mg/kg, which is one-half of the MTD (24 mg/kg) of a single injection. The estimation is consistent with our previous findings. Thus, in this study, the dose of SAPD 1 is 12 mg/kg (one-half MTD). The dose of SAPDs 3 and 4 is 36 mg/kg (one-half MTD). Although SAPD 2 has slightly lower MTD, we also used the same dose as SAPDs 3 and 4 to make them consistent. The irinotecan (i.p. injection; 100 mg/kg at days 1, 8, and 15) and the PBS groups were used as controls. All other protocols were similar to those in the above-mentioned efficacy study.

Data Availability. Necessary materials are available from the corresponding author on reasonable request.

ACKNOWLEDGMENTS. This work is supported by the National Science Foundation CAREER Award (DMR-1255281). The in vivo circulation study in Fig. 5 *D–F* was supported by a grant awarded to P.Z. from National Natural Science Foundation of China (8167808). We acknowledge the Johns Hopkins University (JHU) Integrated Imaging Center TEM facility and the JHU Department of Chemistry Mass Spectrometry Facility.

1. T. Aida, E. W. Meijer, S. I. Stupp, Functional supramolecular polymers. *Science* **335**, 813–817 (2012).
2. M. J. Webber, E. A. Appel, E. W. Meijer, R. Langer, Supramolecular biomaterials. *Nat. Mater.* **15**, 13–26 (2016).
3. M. J. Webber, R. Langer, Drug delivery by supramolecular design. *Chem. Soc. Rev.* **46**, 6600–6620 (2017).
4. M. Elsbahy, G. S. Heo, S. M. Lim, G. Sun, K. L. Wooley, Polymeric nanostructures for imaging and therapy. *Chem. Rev.* **115**, 10967–11011 (2015).
5. H. Acar *et al.*, Self-assembling peptide-based building blocks in medical applications. *Adv. Drug Deliv. Rev.* **110–111**, 65–79 (2017).
6. H. Cui, B. Xu, Supramolecular medicine. *Chem. Soc. Rev.* **46**, 6430–6432 (2017).
7. Z. Feng, T. Zhang, H. Wang, B. Xu, Supramolecular catalysis and dynamic assemblies for medicine. *Chem. Soc. Rev.* **46**, 6470–6479 (2017).
8. D. Peer *et al.*, Nanocarriers as an emerging platform for cancer therapy. *Nat. Nanotechnol.* **2**, 751–760 (2007).
9. L. Su *et al.*, Chemical design of both a glutathione-sensitive dimeric drug guest and a glucose-derived nanocarrier host to achieve enhanced osteosarcoma lung metastatic anticancer selectivity. *J. Am. Chem. Soc.* **140**, 1438–1446 (2018).
10. R. Lin, H. G. Cui, Supramolecular nanostructures as drug carriers. *Curr. Opin. Chem. Eng.* **7**, 75–83 (2015).
11. H. Su, J. M. Koo, H. Cui, One-component nanomedicine. *J. Control. Release* **219**, 383–395 (2015).
12. S. Correa, N. Boehnke, E. Deiss-Yehiely, P. T. Hammond, Solution conditions tune and optimize loading of therapeutic polyelectrolytes into layer-by-layer functionalized liposomes. *ACS Nano* **13**, 5623–5634 (2019).
13. X. Zhao, Z. Poon, A. C. Engler, D. K. Bonner, P. T. Hammond, Enhanced stability of polymeric micelles based on postfunctionalized poly(ethylene glycol)-b-poly(γ -propargyl L-glutamate): The substituent effect. *Biomacromolecules* **13**, 1315–1322 (2012).

14. Y. Bae, S. Fukushima, A. Harada, K. Kataoka, Design of environment-sensitive supramolecular assemblies for intracellular drug delivery: Polymeric micelles that are responsive to intracellular pH change. *Angew. Chem. Int. Ed. Engl.* **42**, 4640–4643 (2003).
15. H. Su, W. Zhang, H. Wang, F. Wang, H. Cui, Paclitaxel-promoted supramolecular polymerization of peptide conjugates. *J. Am. Chem. Soc.* **141**, 11997–12004 (2019).
16. P. Zhang, A. G. Cheetham, Y. A. Lin, H. Cui, Self-assembled Tat nanofibers as effective drug carrier and transporter. *ACS Nano* **7**, 5965–5977 (2013).
17. S. Soukasene *et al.*, Antitumor activity of peptide amphiphile nanofiber-encapsulated camptothecin. *ACS Nano* **5**, 9113–9121 (2011).
18. A. J. Clark *et al.*, CRLX101 nanoparticles localize in human tumors and not in adjacent, nonneoplastic tissue after intravenous dosing. *Proc. Natl. Acad. Sci. U.S.A.* **113**, 3850–3854 (2016).
19. J. Cheng, K. T. Khin, G. S. Jensen, A. Liu, M. E. Davis, Synthesis of linear, beta-cyclodextrin-based polymers and their camptothecin conjugates. *Bioconjug. Chem.* **14**, 1007–1017 (2003).
20. J. Bhattacharyya *et al.*, A paclitaxel-loaded recombinant polypeptide nanoparticle outperforms Abraxane in multiple murine cancer models. *Nat. Commun.* **6**, 7939 (2015).
21. J. Li *et al.*, Dephosphorylation of D-peptide derivatives to form biofunctional, supramolecular nanofibers/hydrogels and their potential applications for intracellular imaging and intratumoral chemotherapy. *J. Am. Chem. Soc.* **135**, 9907–9914 (2013).
22. Y. Gao *et al.*, Enzyme-instructed molecular self-assembly confers nanofibers and a supramolecular hydrogel of Taxol derivative. *J. Am. Chem. Soc.* **131**, 13576–13577 (2009).
23. Y. Shen *et al.*, Prodrugs forming high drug loading multifunctional nanocapsules for intracellular cancer drug delivery. *J. Am. Chem. Soc.* **132**, 4259–4265 (2010).
24. A. G. Cheetham, R. W. Chakroun, W. Ma, H. Cui, Self-assembling prodrugs. *Chem. Soc. Rev.* **46**, 6638–6663 (2017).
25. A. G. Cheetham, P. Zhang, Y. A. Lin, L. L. Lock, H. Cui, Supramolecular nanostructures formed by anticancer drug assembly. *J. Am. Chem. Soc.* **135**, 2907–2910 (2013).
26. J. A. MacKay *et al.*, Self-assembling chimeric polypeptide-doxorubicin conjugate nanoparticles that abolish tumours after a single injection. *Nat. Mater.* **8**, 993–999 (2009).
27. P. Huang *et al.*, Combination of small molecule prodrug and nanodrug delivery: Amphiphilic drug-drug conjugate for cancer therapy. *J. Am. Chem. Soc.* **136**, 11748–11756 (2014).
28. K. Kataoka, A. Harada, Y. Nagasaki, Block copolymer micelles for drug delivery: Design, characterization and biological significance. *Adv. Drug Deliv. Rev.* **47**, 113–131 (2001).
29. X. Tan *et al.*, Light-triggered, self-immolative nucleic acid-drug nanostructures. *J. Am. Chem. Soc.* **137**, 6112–6115 (2015).
30. S. Zhang *et al.*, Poly(ethylene oxide)-block-polyphosphoester-based paclitaxel conjugates as a platform for ultra-high paclitaxel-loaded multifunctional nanoparticles. *Chem. Sci. (Camb.)* **4**, 2122–2126 (2013).
31. X. Hu *et al.*, Polyprodrug amphiphiles: Hierarchical assemblies for shape-regulated cellular internalization, trafficking, and drug delivery. *J. Am. Chem. Soc.* **135**, 17617–17629 (2013).
32. J. Liu *et al.*, Ring-opening polymerization of prodrugs: A versatile approach to prepare well-defined drug-loaded nanoparticles. *Angew. Chem. Int. Ed. Engl.* **54**, 1002–1006 (2015).
33. H. Su *et al.*, Supramolecular crafting of self-assembling camptothecin prodrugs with enhanced efficacy against primary cancer cells. *Theranostics* **6**, 1065–1074 (2016).
34. S. C. Owen, D. P. Y. Chan, M. S. Shoichet, Polymeric micelle stability. *Nano Today* **7**, 53–65 (2012).
35. Y. Zhao *et al.*, Near-infrared fluorescence energy transfer imaging of nanoparticle accumulation and dissociation kinetics in tumor-bearing mice. *ACS Nano* **7**, 10362–10370 (2013).
36. A. B. E. Attia *et al.*, The effect of kinetic stability on biodistribution and anti-tumor efficacy of drug-loaded biodegradable polymeric micelles. *Biomaterials* **34**, 3132–3140 (2013).
37. N. Feiner-Gracia *et al.*, Micellar stability in biological media dictates internalization in living cells. *J. Am. Chem. Soc.* **139**, 16677–16687 (2017).
38. X. Sun *et al.*, The blood clearance kinetics and pathway of polymeric micelles in cancer drug delivery. *ACS Nano* **12**, 6179–6192 (2018).
39. M. Kastantin *et al.*, Thermodynamic and kinetic stability of DSPE-PEG(2000) micelles in the presence of bovine serum albumin. *J. Phys. Chem. B* **114**, 12632–12640 (2010).
40. M. Black *et al.*, Self-assembled peptide amphiphile micelles containing a cytotoxic T-cell epitope promote a protective immune response in vivo. *Adv. Mater.* **24**, 3845–3849 (2012).
41. Z. Feng, H. Wang, X. Chen, B. Xu, Self-assembling ability determines the activity of enzyme-instructed self-assembly for inhibiting cancer cells. *J. Am. Chem. Soc.* **139**, 15377–15384 (2017).
42. Y. Lu *et al.*, Micelles with ultralow critical micelle concentration as carriers for drug delivery. *Nat. Biomed. Eng.* **2**, 318–325 (2018).
43. J. T. Meijer, M. J. A. G. Henkens, I. J. Minten, D. W. P. M. Lowik, J. C. M. van Hest, Disassembling peptide-based fibres by switching the hydrophobic-hydrophilic balance. *Soft Matter* **3**, 1135–1137 (2007).
44. J. T. Meijer *et al.*, Stabilization of peptide fibrils by hydrophobic interaction. *Langmuir* **23**, 2058–2063 (2007).
45. E. Blanco, H. Shen, M. Ferrari, Principles of nanoparticle design for overcoming biological barriers to drug delivery. *Nat. Biotechnol.* **33**, 941–951 (2015).
46. A. G. Cheetham, Y. C. Ou, P. Zhang, H. Cui, Linker-determined drug release mechanism of free camptothecin from self-assembling drug amphiphiles. *Chem. Commun. (Camb.)* **50**, 6039–6042 (2014).
47. E. A. Dubikovskaya, S. H. Thorne, T. H. Pillow, C. H. Contag, P. A. Wender, Overcoming multidrug resistance of small-molecule therapeutics through conjugation with releasable octaarginine transporters. *Proc. Natl. Acad. Sci. U.S.A.* **105**, 12128–12133 (2008).
48. H. Wang *et al.*, Redox-responsive, core-cross-linked micelles capable of on-demand, concurrent drug release and structure disassembly. *Biomacromolecules* **14**, 3706–3712 (2013).
49. H. Su, F. Wang, Y. Wang, A. G. Cheetham, H. Cui, Macrocyclization of a class of camptothecin analogues into tubular supramolecular polymers. *J. Am. Chem. Soc.* **141**, 17107–17111 (2019).
50. P. A. Korevaar, C. Schaefer, T. F. A. de Greef, E. W. Meijer, Controlling chemical self-assembly by solvent-dependent dynamics. *J. Am. Chem. Soc.* **134**, 13482–13491 (2012).
51. W. Zhang *et al.*, Supramolecular linear heterojunction composed of graphite-like semiconducting nanotubular segments. *Science* **334**, 340–343 (2011).
52. A. S. Weingarten *et al.*, Self-assembling hydrogel scaffolds for photocatalytic hydrogen production. *Nat. Chem.* **6**, 964–970 (2014).
53. Y. S. Velichko, S. I. Stupp, M. O. de la Cruz, Molecular simulation study of peptide amphiphile self-assembly. *J. Phys. Chem. B* **112**, 2326–2334 (2008).
54. P. Greenspan, E. P. Mayer, S. D. Fowler, Nile red: A selective fluorescent stain for intracellular lipid droplets. *J. Cell Biol.* **100**, 965–973 (1985).
55. M. C. A. Stuart, J. C. van de Pas, J. B. F. N. Engberts, The use of Nile Red to monitor the aggregation behavior in ternary surfactant-water-organic solvent systems. *J. Phys. Org. Chem.* **18**, 929–934 (2005).
56. Z. Huang *et al.*, Pulsating tubules from noncovalent macrocycles. *Science* **337**, 1521–1526 (2012).
57. H. Cui, M. J. Webber, S. I. Stupp, Self-assembly of peptide amphiphiles: From molecules to nanostructures to biomaterials. *Biopolymers* **94**, 1–18 (2010).
58. L. Haines-Butterick *et al.*, Controlling hydrogelation kinetics by peptide design for three-dimensional encapsulation and injectable delivery of cells. *Proc. Natl. Acad. Sci. U.S.A.* **104**, 7791–7796 (2007).
59. S. Golan *et al.*, Influence of biological media on the structure and behavior of ferrocene-containing cationic lipid/DNA complexes used for DNA delivery. *Langmuir* **27**, 6615–6621 (2011).
60. Y. Pommier, Topoisomerase I inhibitors: Camptothecins and beyond. *Nat. Rev. Cancer* **6**, 789–802 (2006).
61. T. Schluep, J. Cheng, K. T. Khin, M. E. Davis, Pharmacokinetics and biodistribution of the camptothecin-polymer conjugate IT-101 in rats and tumor-bearing mice. *Cancer Chemother. Pharmacol.* **57**, 654–662 (2006).
62. C. L. Messerer *et al.*, Liposomal irinotecan: Formulation development and therapeutic assessment in murine xenograft models of colorectal cancer. *Clin. Cancer Res.* **10**, 6638–6649 (2004).
63. T. C. Chang *et al.*, Phase I study of nanoliposomal irinotecan (PEP02) in advanced solid tumor patients. *Cancer Chemother. Pharmacol.* **75**, 579–586 (2015).
64. H. Zhang, Onivyde for the therapy of multiple solid tumors. *Oncotargets Ther.* **9**, 3001–3007 (2016).
65. H. C. Pitot *et al.*, Phase I dose-finding and pharmacokinetic trial of irinotecan hydrochloride (CPT-11) using a once-every-three-week dosing schedule for patients with advanced solid tumor malignancy. *Clin. Cancer Res.* **6**, 2236–2244 (2000).
66. Y. Geng *et al.*, Shape effects of filaments versus spherical particles in flow and drug delivery. *Nat. Nanotechnol.* **2**, 249–255 (2007).